



HAL
open science

Interplay between Strain and Defects at the Interfaces of Ultra-Thin Hf 0.5 Zr 0.5 O 2 -Based Ferroelectric Capacitors

Greta Segantini, Benoît Manchon, Infante Ingrid C., Matthieu Bugnet, Rabei Barhoumi, Shruti Nirantar, Edwin Mayes, Pedro Rojo Romeo, Nicholas Blanchard, Damien Deleruyelle, et al.

► **To cite this version:**

Greta Segantini, Benoît Manchon, Infante Ingrid C., Matthieu Bugnet, Rabei Barhoumi, et al.. Interplay between Strain and Defects at the Interfaces of Ultra-Thin Hf 0.5 Zr 0.5 O 2 -Based Ferroelectric Capacitors. *Advanced Electronic Materials*, 2023, pp.2300171. 10.1002/aelm.202300171 . hal-04186567

HAL Id: hal-04186567

<https://hal.science/hal-04186567>

Submitted on 26 Nov 2023

HAL is a multi-disciplinary open access archive for the deposit and dissemination of scientific research documents, whether they are published or not. The documents may come from teaching and research institutions in France or abroad, or from public or private research centers.

L'archive ouverte pluridisciplinaire **HAL**, est destinée au dépôt et à la diffusion de documents scientifiques de niveau recherche, publiés ou non, émanant des établissements d'enseignement et de recherche français ou étrangers, des laboratoires publics ou privés.

Interplay between Strain and Defects at the Interfaces of Ultra-Thin $\text{Hf}_{0.5}\text{Zr}_{0.5}\text{O}_2$ -Based Ferroelectric Capacitors

Greta Segantini,* Benoît Manchon, Ingrid Cañero Infante, Matthieu Bugnet, Rabei Barhoumi, Shruti Nirantar, Edwin Mayes, Pedro Rojo Romeo, Nicholas Blanchard, Damien Deleruyelle, Sharath Sriram, and Bertrand Vilquin

Hafnium zirconium oxide (HZO) is an ideal candidate for the implementation of ferroelectric memristive devices, due to its compatibility with the complementary metal-oxide-semiconductor technology. Ferroelectricity in HZO films is significantly influenced by the properties of electrode/HZO interfaces. Here, the impact of the interfacial microstructure and chemistry on the ferroelectricity of 6 nm-thick HZO-based capacitors, realized by sputtering, with titanium nitride or tungsten electrode materials, is investigated. The results highlight a strong correlation between the structural properties of electrode/HZO interfaces and the HZO ferroelectric performance. Interface effects become significant at low HZO thickness, thus the precise control over the quality of electrode/HZO interfaces allows the remarkable improvement of HZO ferroelectric properties. A double remanent polarization of $40 \mu\text{C cm}^{-2}$ is achieved. This work is a new step towards high quality ultra-thin HZO films with enhanced ferroelectricity for the implementation of ferroelectric tunnel junctions for brain-inspired computing.

memristors are extremely promising components for the implementation of beyond-Von Neumann hardware architectures, such as in-memory computing and brain-inspired computing.^[1,2] The discovery of ferroelectricity in Si-doped HfO_2 has paved the way for the integration of ferroelectric-based devices into the complementary metal-oxide-semiconductor (CMOS) industry.^[3] Among dopants, zirconium (Zr) is one of the most investigated.^[4,5] Similarly to HfO_2 , ZrO_2 has been widely used in the micro- and nano-electronic industry, and the $\text{Hf}_{0.5}\text{Zr}_{0.5}\text{O}_2$ compound, through Hf:Zr 1:1 substitution, displays high values of remanent polarization and low crystallization temperature.^[6] The synthesis of HZO films less than 8 nm-thick and the control of the heterostructure properties are crucial for the fabrication


and performances of FTJs. However, this still represents a challenging task, since at low film thickness the nucleation of the non-ferroelectric tetragonal phase is favored compared to the ferroelectric orthorhombic phase.^[7] Numerous studies have been dedicated to enhancing the ferroelectric properties of HZO-based

1. Introduction

The exponential development of artificial intelligence technologies has increased the demand of computing power and energy efficiency. In this respect, ferroelectric tunnel junction (FTJ)

G. Segantini, R. Barhoumi, P. Rojo Romeo, B. Vilquin
Ecole Centrale Lyon, INSA Lyon, UCBL, CPE Lyon, CNRS, INL,
UMR5270
Univ Lyon
Ecully 69130, France
E-mail: greta.segantini@ec-lyon.fr
G. Segantini, S. Nirantar, S. Sriram
Functional Materials and Microsystems Research Group and Micro
Nano Research Facility
RMIT University
Melbourne, VIC 3001, Australia

B. Manchon, D. Deleruyelle
INSA Lyon, Ecole Centrale Lyon, UCBL, CPE Lyon, CNRS, INL,
UMR5270
Univ Lyon
Villeurbanne 69621, France
I. Cañero Infante
CNRS, INSA Lyon, Ecole Centrale Lyon, UCBL, CPE Lyon, INL,
UMR5270
Univ Lyon
Villeurbanne 69621, France
M. Bugnet
CNRS, INSA Lyon, UCBL, MATEIS, UMR 5510
Univ Lyon
Villeurbanne 69621, France
E. Mayes
RMIT Microscopy and Microanalysis Facility
RMIT University
Melbourne, VIC 3001, Australia
N. Blanchard
Institut Lumière Matière, UMR5306
Université Lyon 1-CNRS, Université de Lyon
Villeurbanne 69622, France

 The ORCID identification number(s) for the author(s) of this article can be found under <https://doi.org/10.1002/aelm.202300171>

© 2023 The Authors. Advanced Electronic Materials published by Wiley-VCH GmbH. This is an open access article under the terms of the Creative Commons Attribution License, which permits use, distribution and reproduction in any medium, provided the original work is properly cited.

DOI: 10.1002/aelm.202300171

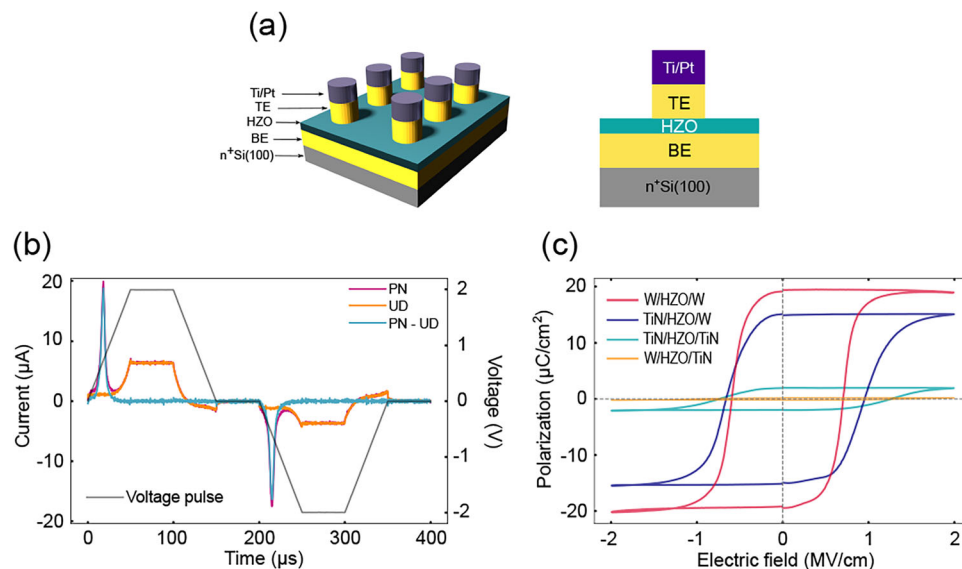


Figure 1. a) Schematic of the structure and the cross-section of the synthesized specimens. b) Current response extracted during a PUND cycle, in gray the waveform used for the PUND measurements and for the device cycling. c) P – E curves of samples TiN/HZO/TiN extracted at 10^5 cycles, TiN/HZO/W extracted at 10^4 cycles, W/HZO/TiN extracted at 10^4 cycles, and W/HZO/W extracted at 10^4 cycles.

devices by optimizing the fabrication conditions and engineering the device structure, with the aim of achieving robust ferroelectric behavior in increasingly thinner films. Among the strategies employed, the choice of electrodes has emerged as a crucial factor. While conductive titanium nitride (TiN) has been extensively investigated as an electrode material for thin HZO-based structures, other literature reports have shown improvements in HZO ferroelectric properties through the use of metal electrodes. Indeed, they have been proposed as a means to enhance the properties of electrode/HZO interfaces, thereby improving the endurance, wake-up, and remanent polarization of the device.^[8–11] Recently, the ferroelectricity in ultra-thin HZO films has been demonstrated down to 1 nm.^[12,13] At this thickness, interface effects become dominant, and precise control of the electrode/HZO interfaces is essential to avoid the degradation of HZO ferroelectric properties. Since the discovery of the ferroelectric phase in doped-HfO₂ in 2011,^[3] the synthesis of HfO₂-based and HZO thin films has been carried out by various deposition techniques such as atomic-layer deposition (ALD)^[6,14–18] and plasma-enhanced ALD (PE-ALD),^[19,20] pulsed-laser deposition (PLD),^[21–25] and sputtering.^[26–32] However, the latter has rarely been used for the deposition of HZO films below 7 nm, for which PLD,^[33–35] ALD,^[13,36] and PE-ALD^[10,37] are employed. Here, we studied four different 6 nm-thick HZO-based heterostructures, which were entirely realized by sputtering, with electrodes made of TiN and/or tungsten (W). We report an exhaustive analysis of the structural and chemical properties of the electrode/ferroelectric interfaces and highlight how they influence the ferroelectric performances of ultra-thin HZO-based devices. Promising results in the synthesis of ferroelectric thin films have been reported in the literature using W as electrode material,^[10,11,38] due to its relatively low thermal expansion coefficient (TEC) compared to the one of TiN ($TEC_W \approx 4.16 \times 10^{-6} \text{ K}^{-1}$), $TEC_{TiN} \approx 8 \times 10^{-6} \text{ K}^{-1}$). In the cited works the ferroelectric films were mainly fabricated using ALD, which may

present some constraints in terms of deposition rates and cost-effectiveness. In contrast, sputtering is an attractive alternative for several reasons, including faster deposition rates, compatibility with room temperature deposition, absence of carbon contamination, and compatibility with industrial processes.^[26,28] In this work, we provide relevant information for the synthesis of ultra-thin HZO films with robust ferroelectricity using sputtering, achieving a state-of-the-art result. These devices could be appropriate for the implementation of FTJs, which could serve as memory units in neuromorphic architectures, where device reliability is fundamental.^[39] For this reason, the improvement of material engineering and optimization of device structure are critical aspects to deal with.

2. Results

2.1. Electrical Characterization

Four heterostructures were investigated: n⁺Si/TiN/HZO/TiN/Ti/Pt, n⁺Si/TiN/HZO/W/Ti/Pt, n⁺Si/W/HZO/TiN/Ti/Pt, and n⁺Si/W/HZO/W/Ti/Pt. For simplicity, they are called TiN/HZO/TiN, TiN/HZO/W, W/HZO/TiN, and W/HZO/W, respectively, in the remainder of the manuscript. **Figure 1a** reports a schematic of the device structure and its cross-section. The Positive-Up-Negative-Down (PUND) technique was employed to measure the polarization versus electric field (P – E) characteristics of the four samples, shown in **Figure 1c**. **Figure 1b** reports the current response of sample W/HZO/W recorded during a PUND pulse train, together with the voltage waveform used for PUND measurements and device cycling. Details on the procedure used to extract the P – E curves can be found in Supporting Information. The double remanent polarization ($2P_r$) of sample TiN/HZO/TiN is $\approx 4 \mu\text{C cm}^{-2}$. It is remarkably higher for samples TiN/HZO/W and W/HZO/W, for which it is ≈ 30 and $\approx 40 \mu\text{C cm}^{-2}$, respectively. On the contrary, $2P_r$

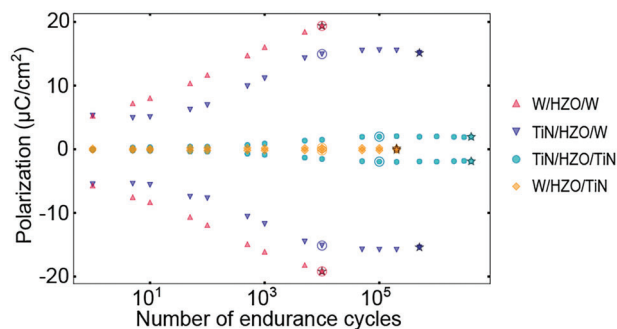


Figure 2. Endurance test of samples TiN/HZO/TiN, TiN/HZO/W, W/HZO/TiN, and W/HZO/W, performed using a cycling voltage of ± 2 V as indicated in Figure 1b. Circles are drawn at the number of cycles at which the P - E curve was extracted, black stars indicate the breakdown point.

does not reach $1 \mu\text{C cm}^{-2}$ in the case of sample W/HZO/TiN. Sample TiN/HZO/TiN is characterized by the largest coercive field (E_c), $\approx \pm 1.5 \text{ MV cm}^{-1}$. E_c values of samples TiN/HZO/W and W/HZO/W are $\approx \pm 1$ and $\approx \pm 0.8 \text{ MV cm}^{-1}$, respectively. An Imprint, which is the tendency of ferroelectric materials to develop a preferred state of polarization resulting in a shift of the center of the hysteresis loop, was detected in both TiN/HZO/TiN and TiN/HZO/W specimens. The difference in the absolute value of the positive and negative coercive field caused by the imprint should ideally be minimized to avoid data loss.^[40,41] In both cases, the imprint is likely associated with structural differences between the top and bottom interfaces, such as different surface terminations and atomic arrangement,^[42,43] since TiN and W are characterized by similar values of the work function, about 4.5 eV .^[44,45]

The evolution of polarization as a function of applied voltage cycles of samples TiN/HZO/TiN, TiN/HZO/W, W/HZO/TiN, and W/HZO/W is reported in Figure 2. The TiN/HZO/TiN sample exhibits the highest endurance of 5×10^6 cycles. The TiN/HZO/W and W/HZO/W samples experience electrical breakdown at 5×10^5 and 10^4 cycles, respectively. Finally, Sample W/HZO/TiN breaks down at $\approx 10^5$ cycles. Unlike the TiN/HZO/TiN sample, the TiN/HZO/W and W/HZO/W heterostructures exhibit ferroelectricity in their pristine state. However, during cycling, they showed a significant increase in P_r , commonly referred to as wake-up, compared to the TiN/HZO/TiN sample. Both the TiN/HZO/W and W/HZO/W structures reach their maximum P_r values after 10^4 cycles. On the other hand, the W/HZO/TiN sample demonstrates an incipient ferroelectric behavior with an undetectable wake-up before experiencing electrical breakdown.

2.2. Structural and Chemical Characterization

Structural and chemical analyses were performed at different length-scales, using glancing incidence X-ray diffraction (GI-XRD) for the whole stack, electron energy-loss spectroscopy (EELS) in scanning transmission electron microscopy (STEM) mode for individual interfaces, and high-resolution TEM (HR-TEM) for the HZO film. This multiscale approach was carried out to study the HZO/electrode interfacial characteristics and the

nanostructure of HZO. The GI-XRD patterns of the four studied specimens are reported in Figure 3a. Reference XRD patterns for TiN, HZO *o*-/*t*-phase, HZO *m*-phase, and the fitting procedure can be found elsewhere.^[46] Each sample displays a peak at $\approx 30.5^\circ$, which indicates the co-presence of orthorhombic and tetragonal phase components, expected at 30.4° (*o*-HZO(111)) and 30.8° (*t*-HZO(101)), respectively.^[47] The monoclinic reflections, *m*-HZO(11-1) at 28.4° and *m*-HZO(111) at 31.6° , are absent. In the considered range, no peaks corresponding to TiN or W were detected. Figure 3b reports the results of the fit of the *o*-/*t*-peak for each specimen and the corresponding calculated *o*-/*t*-phase ratio. Samples TiN/HZO/W and W/HZO/W are characterized by *o*-/*t*-phase > 1 , which implies a predominance of the *o*-phase with respect to the *t*-phase. On the contrary, for samples TiN/HZO/TiN and W/HZO/TiN, the *t*-phase prevails over the *o*-phase. The values observed for the *o*/*t* ratio are in accordance with the PUND data. Sample W/HZO/W, which displays the highest $2P_r$, is also characterized by the highest *o*/*t* ratio. While, for samples TiN/HZO/TiN and W/HZO/TiN, which showed a remarkably poor ferroelectricity, *o*/*t* < 1 . Nevertheless, this analysis is primarily qualitative, and, as pointed out by Shroeder *et al.*,^[48] GI-XRD cannot unambiguously differentiate the orthorhombic contribution from the tetragonal one, and the deconvolution of the *o*-/*t*-phase could be affected by other parameters, that are, strain induced by bottom and top electrode, intrinsic strain produced during the high temperature crystallization process and conditions, and oxygen vacancies content.

In order to gain better insights on the impact of different electrodes on the HZO ferroelectric performances, the microstructure and chemistry of interfaces were investigated at high resolution using STEM-EELS on $10 \mu\text{m}$ -diameter pristine capacitors. The evolution of the O-K edge along the cross-section bottom electrode (BE)/HZO/top electrode (TE) (shown in the high-angle annular dark-field (HAADF) image) of the four studied structures is reported in Figure 4. The O-K edges in Figure 4a,c,e,g were extracted from the electrodes, bottom interface, top interface, and HZO for samples TiN/HZO/TiN, TiN/HZO/W, W/HZO/TiN, and W/HZO/W. The corresponding contour plots of the projected O-K edge intensity along the interfaces are shown in Figure 4b,d,f,h. For the structure TiN/HZO/TiN (Figure 4a,b), the presence of an O-K pre-edge in HZO at bottom and top interfaces is in contrast with the center of the HZO film, where the edge onset is sharper and without pre-edge peaks. The similarity of the O-K near-edge fine structure (ELNES) at the bottom and top interfaces suggests that the chemistry is similar at both interfaces. EELS spectra in the energy-loss range 394–555 eV and of Ti-L_{2,3} edges of samples TiN/HZO/TiN, TiN/HZO/W, and W/HZO/TiN are reported in Figure S6–S9 (Supporting Information). The coexistence of N-K, Ti-L_{2,3}, and O-K edges over few nm at bottom and top interfaces indicates the oxidation of TiN into TiN(O),^[26,46] which is in agreement with earlier reports that the O-K pre-edge features suggest the presence of defects, such as oxygen vacancies in HfO₂,^[49,50] or ZrO₂.^[51,52] The O-K edge fine structures are also very sensitive to crystal field variations induced by structural distortions in the lattice. The occurrence of a pre-edge and fine structure variations were evidenced in highly textured films with extremely low thickness.^[12] Nevertheless, the absence of O-K pre-edge in the middle of the HZO films, and the presence of TiN(O) suggest that such structural distortion

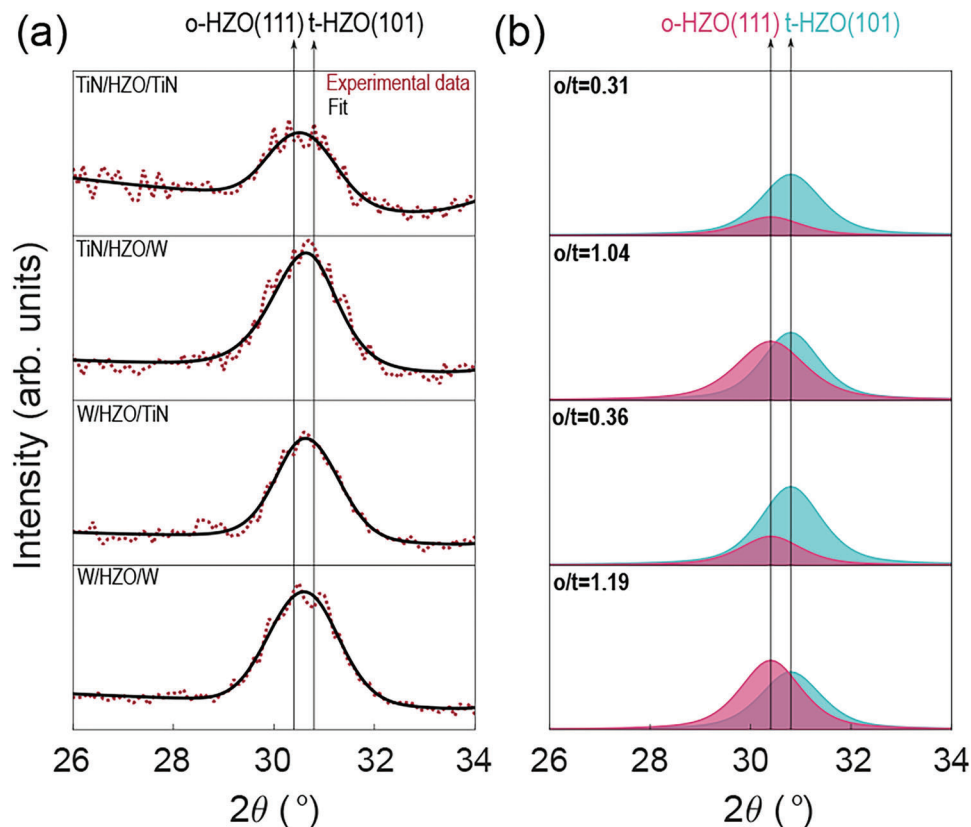


Figure 3. GI-XRD analysis : a) GI-XRD patterns and fits that show intensity versus scattering angle of samples -from top-: TiN/HZO/TiN, TiN/HZO/W, W/HZO/TiN, W/HZO/W. b) Result of the fit of the o-/t-peak for each specimen, at top left the calculated o-/t-phase ratio.

effects play a minor role on the observed pre-edge compared to oxygen vacancies. The same O–K edge fine structure variations are observed at the TiN/HZO interface in samples TiN/HZO/W (Figure 4c,d) and W/HZO/TiN (Figure 4e,f). The difference between HZO/W and HZO/TiN interfaces is remarkable, as highlighted in the extracted edges in Figure 4c,e, and in the contour plots in Figure 4d,f. The O–K ELNES in HZO at the HZO/W interface is comparable to the centre of the HZO film and fades once W is reached. This observation indicates that the creation of oxygen vacancies in HZO at the HZO/W interface is much less prominent than at the HZO/TiN interface. Similar conclusions are reached for the sample W/HZO/W. The fine structures of the O–K edge, which reflect the local electronic structure around oxygen atoms, of the HZO layer are characterized by two distinct peaks, light blue line in Figure 4a,c,e,g. These are due to metal e_g - t_{2g} splitting of the Hf $5d$ bands.^[50,53] The ratio between the high-energy peak (≈ 537 eV) and low-energy peak (≈ 533 eV), as well as the peak splitting differ for each specimen. Samples TiN/HZO/W and W/HZO/W are characterized by a small ratio and a clear splitting. On the contrary, a larger ratio and a less defined peak splitting mark structures TiN/HZO/TiN and W/HZO/TiN. The latter features can be associated with an oxygen-deficient HZO,^[54] and they were demonstrated in oxygen-deficient HfO₂ as well.^[55] In conclusion, TiN as a TE seems to be responsible for more efficient oxygen scavenging from the HZO layer with respect to W TE. This result acts as a further explanation

for the appearance of a TiN(O) interlayer at the HZO/TiN (TE) interface.

HR-TEM was employed to investigate the nanostructure of the cross-section BE/HZO/TE and the local in-plane grain size of the HZO layer. HR-TEM images of structures TiN/HZO/TiN, TiN/HZO/W, W/HZO/TiN, and W/HZO/W are displayed in Figure 5. In each image, the grain boundaries are marked with red triangles. Samples TiN/HZO/W and W/HZO/W (Figure 5b,d) are characterized by smaller in-plane grains compared to structures TiN/HZO/TiN and W/HZO/TiN (Figure 5a,c). HR-TEM revealed that a large in-plane grain size seem to be correlated with poor ferroelectric performances, in agreement with some reports in literature, which showed that large grains can induce the formation of high symmetry phases such as m- and t-phases.^[31,56,57] Furthermore, Lee *et al.* observed that even minor variations in grain size, in thin films prepared by sputtering, notably influence their ferroelectric behavior.^[31] From the HR-TEM analysis, it was not possible to clearly distinguish the interfacial layer formed at the HZO/TiN interface. However, its presence is evinced by the STEM-EELS chemical analysis, where the evolution of the O–K edge fine structures (in Figure 4c,e) indicates a higher oxidation of the TiN electrode at the HZO/TiN interface with respect to the W electrode at the HZO/W one. This observation is supported by the HAADF images shown in Figure S5 (Supporting Information).

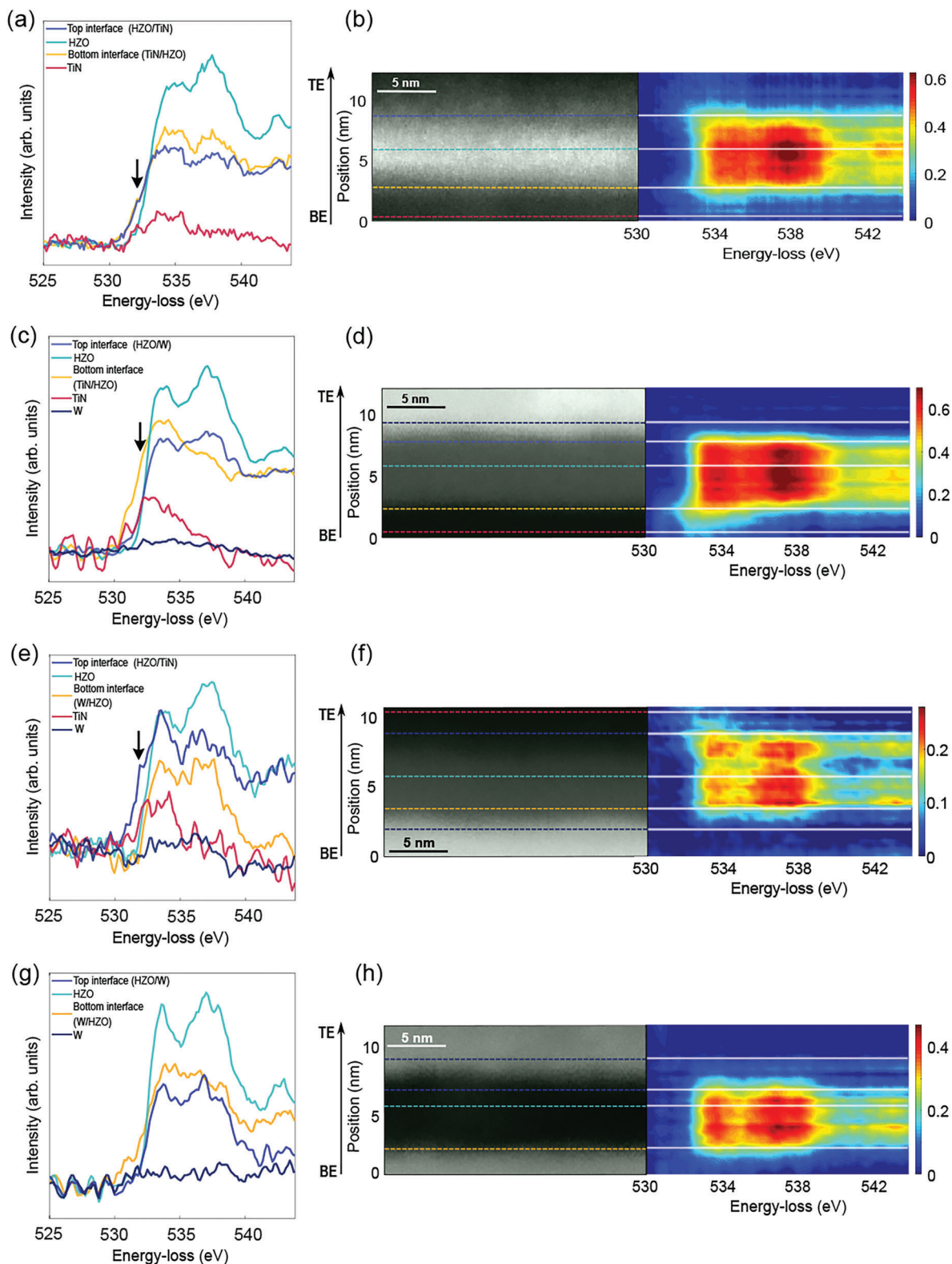


Figure 4. EELS analysis: a) EELS O-K edge of sample TiN/HZO/TiN extracted in HZO, TiN BE, at bottom interface, and top interface. b) On the left, STEM-HAADF image of the cross-section BE/HZO/TE, dashed color lines correspond to the positions where spectra in (a) were extracted. On the right, EELS O-K edges, represented in a contour plot, extracted along the cross-section BE/HZO/TE. Same for sample TiN/HZO/W c,d), W/HZO/TiN e,f), and W/HZO/W g,h). The arrows indicate the position of the pre-edge.

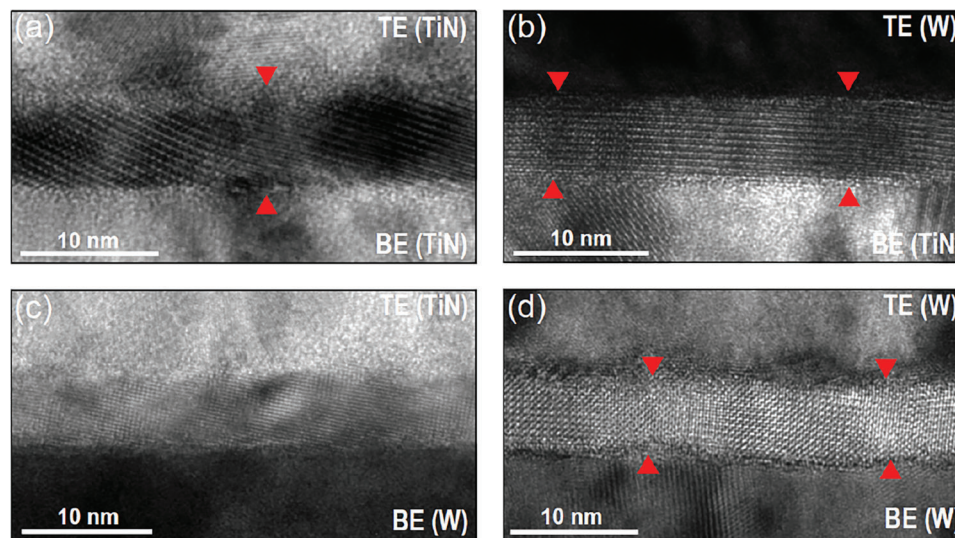


Figure 5. HR-TEM images of samples: a) TiN/HZO/TiN, b) TiN/HZO/W, c) W/HZO/TiN, d) W/HZO/W. Grain boundaries are identified by red triangles in each image.

Table 1 summarizes the characteristics discussed for each studied heterostructure.

3. Discussion

This study reveals the importance of the chemistry and structure of interfaces on the ferroelectric properties of ultra-thin HZO films. W TE guarantees better ferroelectric performances compared to TiN TE, when ultra-thin HZO films (<7 nm) are considered. This result confirms some reports in literature.^[11,38,58–60] One of the reasons for this is attributed to the lower TEC of W ($\approx 4.16 \times 10^{-6} \text{ K}^{-1}$) compared to the one of HZO ($\approx 7 \times 10^{-6} \text{ K}^{-1}$), which is responsible for an in-plane thermal strain in the cooling phase post-annealing.^[11] At this stage, the TE plays a crucial role in the o-phase formation. Indeed, it provides a stronger mechanical confinement compared to the BE, which prevents the transition from the t- to m-phase and promotes the transition from the t- to o-phase, as it is also confirmed by the GI-XRD patterns, where monoclinic peaks are nearly absent. Only a weak monoclinic reflection is observed at $\approx 35.5^\circ$ (Figure S3, Supporting Information). This phenomenon, known as the “capping” effect, has been extensively documented in the literature through various studies.^[61,62] The latter effect could be attenuated in the case

of the TiN TE, which is characterized by a TEC of $\approx 8 \times 10^{-6} \text{ K}^{-1}$, similar to the one of HZO.

Furthermore, in the study of the HZO/TE interface, the STEM-EELS analysis showed a lower oxidation of HZO/W interface with respect to HZO/TiN one, in accordance with other works,^[38] which suggests a reduction of the dead-layer thickness at the former interface compared to the latter. In the literature, it has been reported that the formation of an interfacial dielectric layer is among the first causes of degradation of ferroelectricity.^[58] In the case of sample TiN/HZO/W, STEM-EELS data revealed the presence of an interfacial layer at TiN/HZO bottom interface, due to oxygen scavenging.^[26,63,64] However, we concluded that both in-plane strain from W TE and a thin dead-layer at the HZO/W top interface were the key factors that notably improved the ferroelectric properties of samples TiN/HZO/W and W/HZO/W, where an extremely high value of switchable polarization was reached.

Nonetheless, oxygen scavenging by the TiN electrodes generates oxygen vacancies, which have proven to be beneficial for the stabilization of o-phase against t-phase in thin HZO films.^[65,66] We hypothesized that, in the case of sample TiN/HZO/TiN, the role of oxygen vacancies was hindered by the interfacial dead-layers at top and bottom interfaces (Figure 4a,b), which reduced the thickness of the active layer. Moreover, it has been shown that a high concentration of oxygen vacancies might lead to the

Table 1. Summary of the characteristics of the studied heterostructures.

Sample	TiN/HZO/TiN	TiN/HZO/W	W/HZO/TiN	W/HZO/W
Maximum $2P_r$ (μCcm^{-2})	4	30	1	40
Endurance (cycles)	5×10^6	5×10^5	10^5	10^4
o/t ratio	0.31	1.04	0.36	1.19
State of bottom interface	High oxidation	High oxidation	Low oxidation	Low oxidation
State of top interface	High oxidation	Low oxidation	High oxidation	Low oxidation
In-plane grain size (nm), estimated from HR-TEM	≈ 20	$\approx 10\text{--}20$	> 20	$\approx 10\text{--}15$

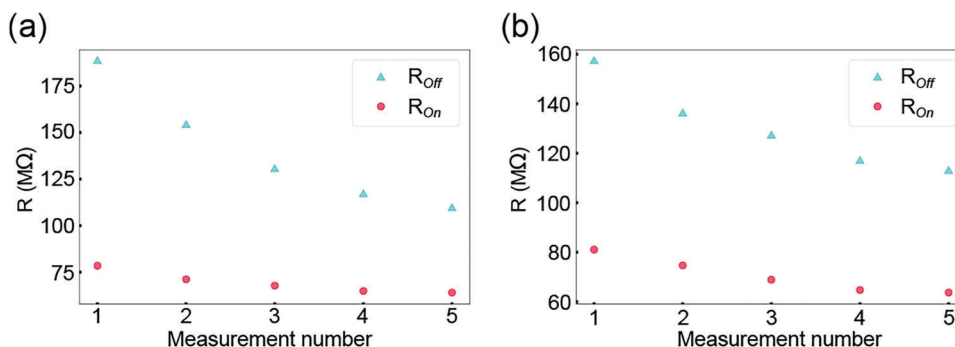


Figure 6. a) Measured On resistance (R_{On}) and Off resistance (R_{Off}) for applied positive voltage. b) Measured R_{On} and R_{Off} for applied negative voltage, for sample W/HZO/W.

formation of t-phase,^[31,65] which is supported by the value of the o/t ratio reported in Figure 3b. These observations could explain the low value of remanent polarization of the structure TiN/HZO/TiN.

Within the context of structural analysis, the weak ferroelectricity observed in the W/HZO/TiN sample can be attributed to multiple factors. First, it has been demonstrated that thin films with a high oxygen content tend to have larger grains compared to those with lower oxygen content.^[31] W BE scavenges less oxygen from the HZO layer compared to TiN (Figure 4), resulting in a higher oxygen content within the HZO layer, potentially leading to the formation of large grains (Table 1). Second, the TiN TE scavenges more oxygen from the HZO layer compared to the W TE, resulting in a lower oxygen content near the top interface, which might promote the formation of the t-phase.^[31,65] Additionally, as previously mentioned, the oxygen scavenging process generates a non-ferroelectric interfacial layer (as shown in Figure 5c) that reduces the thickness of the active layer. Lastly, the insufficient in-plane strain provided by the TiN TE diminishes the “capping” effect. Based on these observations, we hypothesized that

the combination of these factors contribute to the poor ferroelectric behavior of the W/HZO/TiN sample. Conversely, in the case of the W/HZO/W sample, the strong mechanical confinement induced by the W TE may modify the grain size, leading to better ferroelectric performances. As aforementioned, even small variations in grain dimensions can have a significant impact on the ferroelectric response.^[31]

In terms of endurance, the observed low value for the W/HZO/W sample, while consistent with previous reports on similar structures,^[11] may stem from several factors. The high value of remanent polarization ($40 \mu\text{C cm}^{-2}$) suggests the generation of large electric fields during polarization switching, which can lead to an early electrical breakdown of the sample. Additionally, the lower oxidation of the HZO/W interface compared to the HZO/TiN interface results in a thinner dead-layer in the former case, potentially contributing to a higher effective electric field applied to the ferroelectric film.^[31] Also, metal electrodes have been shown to restrict the movement of oxygen vacancies, which tend to accumulate at the interfacial region and increase leakage current.^[67,68] Finally, some studies have also reported

Table 2. Thin films growth and annealing conditions.

		Sputtering Process		
Target-substrate distance		8 cm		
Base pressure		$<5 \times 10^{-7}$ mbar		
Ignition pressure		5×10^{-2} mbar		
Deposited elements	TiN	$\text{Hf}_{0.5}\text{Zr}_{0.5}\text{O}_2$	W	Pt
Target (purity)	Ti (99,995 %)	$\text{ZrO}_2/\text{HfO}_2$ (50%/50%)	W(99,995 %)	Pt (99.95 %)
Target RF power/voltage (W/V)	300 W	100 W	200 W	137 V
Holder DC bias voltage (V)	60 V	None	None	None
Gas (sccm)	Ar 50 sccm; N ₂ 3 sccm	Ar 50 sccm	Ar 50 sccm	Ar 50 sccm
Working pressure (mbar)	5×10^{-3} mbar	5×10^{-2} mbar	5×10^{-3} mbar	5×10^{-3} mbar
Deposition rate	$\approx 5 \text{ nm min}^{-1}$	$\approx 4 \text{ nm min}^{-1}$	$\approx 25 \text{ nm min}^{-1}$	$\approx 17 \text{ nm min}^{-1}$
		Rapid Thermal Annealing Conditions	Can “Rapid thermal annealing conditions” be written like “Sputtering process”?	
Temperature ($^{\circ}\text{C}$)		450 $^{\circ}\text{C}$		
Atmosphere (1 atm)		N ₂		
Time (s)		30 s		

diffusion of W atoms from the W BE into the HZO films, which further enhances the leakage contribution.^[11,69] In the latter cases, however, the HZO layer was synthesized by PE-ALD and ALD, which can considerably affect the bottom interface.^[67] On the contrary, in this work, where sputtering was employed for HZO deposition, EELS revealed a relatively thin interfacial layer. These findings demonstrate how heterostructures synthesized using different deposition methods exhibit distinct interfacial properties that significantly influence the ferroelectric behavior of ultra-thin HZO. Varying deposition techniques might result in differences in HZO growth, oxygen content, and strain induced by the electrodes. In conclusion, both samples W/HZO/W and TiN/HZO/W are characterized by a significant wake-up, which we ascribed to the presence of defects, such as oxygen vacancies, and a high density of grain boundaries (Figure 5b,d) associated with small grains (Table 1) that might be responsible for domain pinning. During the device cycling, the redistribution of such defects increases the number of domains available for switching, which explains the high rise of P_r .^[70,71]

Finally, static current versus voltage (I - V) measurements indicated the presence of an electroresistance ratio (ER) observed in sample W/HZO/W (the used protocol is available in Supporting Information). **Figure 6** shows the values of O_n resistance (R_{On}) and O_{off} resistance (R_{Off}), measured for applied positive (Figure 6a) and negative (Figure 6b) voltage, for five repetitions of I - V measurements. This result highlights that device structure and electrode/HZO interface properties are critical parameters to optimize for the synthesis of FTJs, and for a further scaling of the thickness of sputtered HZO films. The latter aspect would enhance the contributions of the tunnel currents, in order to achieve high ER ratios.^[33,72]

4. Conclusion

In conclusion, we demonstrated the major role played by structural and physical properties of interfaces in the stabilization of the orthorhombic phase in 6 nm-thick $\text{Hf}_{0.5}\text{Zr}_{0.5}\text{O}_2$ films. Samples with W top electrode showed a significant improvement of the ferroelectric performances compared to structures with TiN top electrode. W induces a larger in-plane tensile strain with respect to TiN, which promotes the formation of the o-phase. Furthermore, the low oxidation of the HZO/W interface was correlated to a thin interfacial dead-layer. This work provides new insights into the chemical and structural nature of electrode/HZO interfaces and how they influence the ferroelectric behavior of HZO films. Furthermore, it clearly shows that an appropriate control over the quality of interfaces is decisive to achieve reliable HZO-based devices and to scale down the HZO thickness, for the synthesis and usability of tunnelling devices for neuro-morphic applications.

5. Experimental Section

Fabrication: Prior to growth, n^+ -Si(100) substrates were cleaned in acetone and ethanol, and the native oxide layer was removed by a buffer oxide etching procedure. All the depositions were performed by magnetron sputtering at room temperature by means of an AC-450 Alliance Concept set up. All the electrodes here mentioned were 50 nm-thick. TiN electrodes

were deposited by reactive sputtering from a Ti target in a mixture of Ar and N_2 at a pressure of 5×10^{-3} mbar. W electrodes and the 6 nm-thick HZO layer were synthesized by sputtering from a W target at a pressure of 5×10^{-3} mbar and from a $\text{Hf}_{0.5}\text{Zr}_{0.5}\text{O}_2$ ceramic target at a pressure of 5×10^{-2} mbar, respectively. UV lithography was carried out to define the capacitor structures after the growth of the bottom electrode and HZO layer, the used procedure was reported elsewhere.^[46] Following the deposition of the top electrode, a protective conductive film made of a few nm-thick Ti adhesive layer and 50 nm of Pt was grown. After a lift-off process, the post-metallization annealing was performed by rapid thermal annealing at 450° for 30 s, in a N_2 (100 %) atmosphere. The growth parameters of HZO layer, BE, TE, and top contact, together with the annealing conditions are reported in **Table 2**.

Characterization: The structural characterization was carried out by glancing-incidence X-ray diffraction (GI-XRD) by means of a five-circle goniometer Smartlab Rigaku diffractometer, using a 9 kW copper rotating anode. GI-XRD experiments were performed using a parabolic multilayer mirror for parallel beam setting, Ni filter for Cu K α radiation selection, 0.114° aperture parallel slit analyser, and a 0D scintillating counter. The electronic structure of electrode/HZO interfaces was probed by electron energy-loss spectroscopy (EELS) in the scanning transmission electron microscope (STEM). The microscope used was a JEOL JEM-F200, equipped with a high-brightness cold field emission gun, and operated at 200 kV. Core-loss STEM-EELS data were collected with a Gatan Continuum S spectrometer using the spectrum-imaging technique implemented in the Gatan microscopy suite, with a dispersion of 0.15 eV per channel. The HR-TEM images were recorded using a JEOL JEM-F200 microscope and a JEOL JEM 2100 (HT pole piece) microscope both operated at 200 kV. The cross-section specimens for STEM analysis were prepared by the Ga-focused ion beam (FIB) milling technique. Polarization versus electric field measurements (P - E) were carried out on 20 μm -diameter capacitors, using a Keithley 4200A-SCS semiconductor parameter analyzer. The electrical characterizations were performed using a manual probe station, where the samples were kept in a closed environment and the electrical contact was made with two tungsten-tip probes. The voltage was applied by direct mechanical contact of the Pt top conductive layer of each device with one probe, while the other was kept on the common bottom electrode. P - E curves were obtained by the positive-up-negative-down (PUND) technique, which consists of a train of five pulses. A negative reset pulse was applied to initialize the polarization along one direction, subsequently two positive (P and U) and two negative pulses (N and D) were applied. The endurance test was performed by cycling the capacitors, usually until electrical breakdown. Static current versus voltage (I - V) measurements were acquired by means of an Agilent 4156B semiconductor parameter analyzer and the measurements were performed by the application of a step-shaped voltage waveform from 0 to ± 2 V. All electrical measurements were carried out at room temperature (300 K).

Supporting Information

Supporting Information is available from the Wiley Online Library or from the author.

Acknowledgements

This work was realized on the NanoLyon technology platform and on the Micro Nano Research Facility at RMIT University. It was funded by the European Union's Horizon 2020 research and innovation programme under Grant Agreement No. 780302 (3eFERRO), by the I3E ECLAUSion project that has received funding from the European Union's Horizon 2020 research and innovation programme under the Marie Skłodowska-Curie grant agreement No. 801512, by the French Public Authorities through the NANO 2022 program, and by International Associated Laboratory in Photonics between France and Australia (LIA ALPhFA). The STEM-EELS and HR-TEM work was performed at the RMIT Microscopy and Microanalysis Facility, a linked laboratory of Microscopy, Australia. Complementary

TEM and HR-TEM experiments were performed at the consortium Lyon-St-Etienne de microscopie and at Institut Lumière Matière. The authors acknowledge Dr. Matthew R. Field and Suvankar Sen from RMIT University for the FIB TEM lamella preparation.

Conflict of Interest

The authors declare no conflict of interest.

Data Availability Statement

The data that support the findings of this study are available from the corresponding author upon reasonable request.

Keywords

electrode/HZO interfaces, ferroelectricity, HZO, thin-films

Received: March 15, 2023

Revised: July 6, 2023

Published online:

- [1] R. Berdan, T. Marukame, K. Ota, M. Yamaguchi, M. Saitoh, S. Fujii, J. Deguchi, Y. Nishi, *Nat. Electron.* **2020**, *3*, 259.
- [2] R. Yang, *Nat. Electron.* **2020**, *3*, 237.
- [3] T. S. Böske, J. Müller, D. Bräuhäus, U. Schröder, U. Böttger, *Appl. Phys. Lett.* **2011**, *99*, 10.
- [4] J. Müller, T. S. Böske, U. Schröder, S. Mueller, D. Bräuhäus, U. Böttger, L. Frey, T. Mikolajick, *Nano Lett.* **2012**, *12*, 4318.
- [5] M. H. Park, H. J. Kim, Y. J. Kim, Y. H. Lee, T. Moon, K. D. Kim, S. D. Hyun, F. Fengler, U. Schroeder, C. S. Hwang, *ACS Appl. Mater. Interfaces* **2016**, *8*, 15466.
- [6] J. Müller, T. S. Böske, D. Bräuhäus, U. Schröder, U. Böttger, J. Sundqvist, P. Kcher, T. Mikolajick, L. Frey, *Appl. Phys. Lett.* **2011**, *99*, 112901.
- [7] M. H. Park, H. J. Kim, Y. J. Kim, Y. H. Lee, T. Moon, K. D. Kim, S. D. Hyun, C. S. Hwang, *Appl. Phys. Lett.* **2015**, *107*, 192907.
- [8] R. Cao, Q. Liu, M. Liu, B. Song, D. Shang, Y. Yang, Q. Luo, S. Wu, Y. Li, Y. Wang, H. Lv, *IEEE Electron Device Lett.* **2019**, *40*, 1744.
- [9] C. Zacharakis, P. Tsipis, S. Chaitoglou, S. Fragkos, M. Axiotis, A. Lagoyiannis, R. Negrea, L. Pintilie, A. Dimoulas, *Appl. Phys. Lett.* **2019**, *114*, 11.
- [10] Y. Goh, J. Hwang, Y. Lee, M. Kim, S. Jeon, *Appl. Phys. Lett.* **2020**, *117*, 242901.
- [11] A. Kashir, H. Kim, S. Oh, H. Hwang, *ACS Appl. Electron. Mater.* **2021**, *3*, 629.
- [12] S. S. Cheema, D. Kwon, N. Shanker, R. dos Reis, S. L. Hsu, J. Xiao, H. Zhang, R. Wagner, A. Datar, M. R. McCarter, C. R. Serrao, A. K. Yadav, G. Karbasian, C. H. Hsu, A. J. Tan, L. C. Wang, V. Thakare, X. Zhang, A. Mehta, E. Karapetrova, R. V. Chopdekar, P. Shafer, E. Arenholz, C. Hu, R. Proksch, R. Ramesh, J. Ciston, S. Salahuddin, *Nature* **2020**, *580*, 478.
- [13] S. S. Cheema, N. Shanker, C. Hsu, A. Datar, J. Bae, D. Kwon, S. Salahuddin, *Adv. Electron. Mater.* **2022**, *8*, 2100499.
- [14] M. Pešić, F. P. G. Fengler, L. Larcher, A. Padovani, T. Schenk, E. D. Grimley, X. Sang, J. M. LeBeau, S. Slesazeck, U. Schroeder, T. Mikolajick, *Adv. Funct. Mater.* **2016**, *26*, 4601.
- [15] Y. Lee, H. Alex Hsain, S. S. Fields, S. T. Jaszewski, M. D. Horgan, P. G. Edgington, J. F. Ihlefeld, G. N. Parsons, J. L. Jones, *Appl. Phys. Lett.* **2021**, *118*, 012903.
- [16] J. Mohan, H. Hernandez-Arriaga, Y. C. Jung, T. Onaya, C. Y. Nam, E. H. Tsai, S. J. Kim, J. Kim, *Appl. Phys. Lett.* **2021**, *118*, 18.
- [17] A. G. Chernikova, A. M. Markeev, *Appl. Phys. Lett.* **2021**, *119*, 032902.
- [18] F. Zhang, Z. D. Luo, Q. Yang, J. Zhou, J. Wang, Z. Zhang, Q. Fan, Y. Peng, Z. Wu, F. Liu, S. Chen, D. He, H. Yin, G. Han, Y. Liu, Y. Hao, *ACS Appl. Mater. Interfaces* **2022**, *14*, 11028.
- [19] T. Onaya, T. Nabatame, N. Sawamoto, A. Ohi, N. Ikeda, T. Nagata, A. Ogura, *Microelectron. Eng.* **2019**, *215*, 111013.
- [20] H.-G. Kim, D.-H. Hong, J.-H. Yoo, H.-C. Lee, *Nanomaterials* **2022**, *12*, 548.
- [21] J. Lyu, I. Fina, F. Sánchez, *Appl. Phys. Lett.* **2020**, *117*, 072901.
- [22] L. Bégon-Lours, M. Mulder, P. Nukala, S. De Graaf, Y. A. Birkhölzer, B. Kooi, B. Noheda, G. Koster, G. Rijnders, *Phys. Rev. Mater.* **2020**, *4*, 043401.
- [23] Y. Wei, P. Nukala, M. Salverda, S. Matzen, H. J. Zhao, J. Momand, A. S. Everhardt, G. Agnus, G. R. Blake, P. Lecoœur, B. J. Kooi, J. Íñiguez, B. Dkhil, B. Noheda, *Nat. Mater.* **2018**, *17*, 1095.
- [24] P. Nukala, J. Antoja-Lleonart, Y. Wei, L. Yedra, B. Dkhil, B. Noheda, *ACS Appl. Electron. Mater.* **2019**, *1*, 2585.
- [25] P. Nukala, Y. Wei, V. de Haas, Q. Guo, J. Antoja-Lleonart, B. Noheda, *Ferroelectrics* **2020**, *569*, 148.
- [26] J. Bouaziz, P. Rojo Romeo, N. Baboux, R. Negrea, L. Pintilie, B. Vilquin, *APL Mater.* **2019**, *7*, 8.
- [27] J. Bouaziz, P. R. Romeo, N. Baboux, B. Vilquin, *ACS Appl. Electron. Mater.* **2019**, *1*, 1740.
- [28] J. Bouaziz, P. Rojo Romeo, N. Baboux, B. Vilquin, *J. Vac. Sci. Technol. B* **2019**, *37*, 021203.
- [29] T. H. Ryu, D. H. Min, S. M. Yoon, *J. Appl. Phys.* **2020**, *128*, 074102.
- [30] L. Baumgarten, T. Szyjka, T. Mittmann, M. Materano, Y. Matveyev, C. Schlueter, T. Mikolajick, U. Schroeder, M. Müller, *Appl. Phys. Lett.* **2021**, *118*, 3.
- [31] Y. H. Lee, H. J. Kim, T. Moon, K. D. Kim, S. D. Hyun, H. W. Park, Y. B. Lee, M. H. Park, C. S. Hwang, *Nanotechnology* **2017**, *28*, 30.
- [32] B. Manchon, G. Segantini, N. Baboux, P. Rojo Romeo, R. Barhoumi, I. C. Infante, F. Alibart, D. Drouin, B. Vilquin, D. Deleruyelle, *Phys. Status Solidi RRL* **2022**, *16*, 2100585.
- [33] M. Cervo Sulzbach, H. Tan, S. Estandía, J. Gàzquez, F. Sánchez, I. Fina, J. Fontcuberta, *ACS Appl. Electron. Mater.* **2021**, *3*, 3657.
- [34] M. C. Sulzbach, S. Estandía, X. Long, J. Lyu, N. Dix, J. Gàzquez, M. F. Chisholm, F. Sánchez, I. Fina, J. Fontcuberta, *Adv. Electron. Mater.* **2020**, *6*, 1900852.
- [35] M. C. Sulzbach, S. Estandía, J. Gàzquez, F. Sánchez, I. Fina, J. Fontcuberta, *Adv. Funct. Mater.* **2020**, *30*, 32.
- [36] G. Walters, A. Shekhawat, N. G. Rudawski, S. Moghaddam, T. Nishida, *Appl. Phys. Lett.* **2018**, *112*, 19.
- [37] P. Jiao, Z. Xi, X. Zhang, Y. Han, Y. Wu, D. Wu, *Appl. Phys. Lett.* **2021**, *118*, 252901.
- [38] G. Karbasian, R. dos Reis, A. K. Yadav, A. J. Tan, C. Hu, S. Salahuddin, *Appl. Phys. Lett.* **2017**, *111*, 022907.
- [39] A. Mehonic, A. Sebastian, B. Rajendran, O. Simeone, E. Vasilaki, A. J. Kenyon, *Adv. Intell. Syst.* **2020**, *2*, 2000085.
- [40] D. Damjanovic, *Rep. Prog. Phys.* **1998**, *61*, 1267.
- [41] J. Bouaziz, P. Rojo Romeo, N. Baboux, B. Vilquin, *Appl. Phys. Lett.* **2021**, *118*, 082901.
- [42] Y. Z. Wu, *J. Appl. Phys.* **2012**, *112*, 5.
- [43] P. Sun, Y. Z. Wu, S. H. Zhu, T. Y. Cai, S. J. J. *Appl. Phys.* **2013**, *113*, 17.
- [44] E. W. Müller, *J. Appl. Phys.* **1955**, *26*, 732.
- [45] S. A. Vitale, J. Kedzierski, P. Healey, P. W. Wyatt, C. L. Keast, *IEEE Trans. Electron Devices* **2011**, *58*, 419.
- [46] G. Segantini, R. Barhoumi, B. Manchon, I. Cañero Infante, P. Rojo Romeo, M. Bugnet, N. Baboux, S. Nirantar, D. Deleruyelle, S. Sriram, B. Vilquin, *Phys. Status Solidi RRL* **2022**, *16*, 2100583.
- [47] M. Hyuk Park, H. Joon Kim, Y. Jin Kim, W. Lee, T. Moon, C. Seong Hwang, *Appl. Phys. Lett.* **2013**, *102*, 242905.

- [48] U. Schroeder, R. Sachdeva, P. D. Lomenzo, B. Xu, M. Materano, T. Mikolajick, A. Kersch, *J. Appl. Phys.* **2022**, 132, 21.
- [49] B. J. Murdoch, D. G. McCulloch, R. Ganesan, D. R. McKenzie, M. M. Bilek, J. G. Partridge, *Appl. Phys. Lett.* **2016**, 108, 14.
- [50] G. D. Wilk, D. A. Muller, *Appl. Phys. Lett.* **2003**, 83, 3984.
- [51] S. Ramanathan, D. A. Muller, G. D. Wilk, C. M. Park, P. C. McIntyre, *Appl. Phys. Lett.* **2001**, 79, 3311.
- [52] S. Ostanin, A. J. Craven, D. W. McComb, D. Vlachos, A. Alavi, M. W. Finnis, A. T. Paxton, *Phys. Rev. B: Condens. Matter Mater. Phys.* **2000**, 62, 14728.
- [53] S. Stemmer, Z. Q. Chen, W. J. Zhu, T. P. Ma, *J. Microsc.* **2003**, 210, 74.
- [54] J. Lee, M. S. Song, W. S. Jang, J. Byun, H. Lee, M. H. Park, J. Lee, Y. M. Kim, S. C. Chae, T. Choi, *Adv. Mater. Interfaces* **2022**, 9, 2101647.
- [55] K. Lee, K. Park, H. J. Lee, M. S. Song, K. C. Lee, J. Namkung, J. H. Lee, J. Park, S. C. Chae, *Sci. Rep.* **2021**, 11, 6290.
- [56] R. Materlik, C. Kunneth, A. Kersch, *J. Appl. Phys.* **2015**, 117, 134109.
- [57] M. Hoffmann, U. Schroeder, T. Schenk, T. Shimizu, H. Funakubo, O. Sakata, D. Pohl, M. Drescher, C. Adelman, R. Materlik, A. Kersch, T. Mikolajick, *J. Appl. Phys.* **2015**, 118, 072006.
- [58] S. Oh, H. Kim, A. Kashir, H. Hwang, *Appl. Phys. Lett.* **2020**, 117, 25.
- [59] X. Lyu, M. Si, X. Sun, M. A. Capano, H. Wang, P. Ye, presented at *2019 Sympos. on VLSI Technol.*, IEEE, Kyoto, Japan, ISBN 978-4-86348-719-2, ISSN 07431562, **2019**
- [60] M. Si, X. Lyu, P. R. Shrestha, X. Sun, H. Wang, K. P. Cheung, P. D. Ye, *Appl. Phys. Lett.* **2019**, 115, 072107.
- [61] R. Cao, Y. Wang, S. Zhao, Y. Yang, X. Zhao, W. Wang, X. Zhang, H. Lv, Q. Liu, M. Liu, *IEEE Electron Device Lett.* **2018**, 39, 1207.
- [62] Y. H. Lee, S. D. Hyun, H. J. Kim, J. S. Kim, C. Yoo, T. Moon, K. D. Kim, H. W. Park, Y. B. Lee, B. S. Kim, J. Roh, M. H. Park, C. S. Hwang, *Adv. Electron. Mater.* **2019**, 5, 1800436.
- [63] S. J. Kim, J. Mohan, H. S. Kim, S. M. Hwang, N. Kim, Y. C. Jung, A. Sahota, K. Kim, H. Y. Yu, P. R. Cha, C. D. Young, R. Choi, J. Ahn, J. Kim, *Materials* **2020**, 13, 2968.
- [64] A. A. Koroleva, A. G. Chernikova, S. S. Zarubin, E. Korostylev, R. R. Khakimov, M. Y. Zhuk, A. M. Markeev, *ACS Omega* **2022**, 7, 47084.
- [65] T. Mittmann, M. Materano, S. C. Chang, I. Karpov, T. Mikolajick, U. Schroeder, presented at *Technical Digest - Int. Electron Devices Meeting, IEDM*, IEEE, Piscataway, NJ, USA **2020**, pp. 18.4.1.
- [66] T. Mittmann, M. Michailow, P. D. Lomenzo, J. Gärtner, M. Falkowski, A. Kersch, T. Mikolajick, U. Schroeder, *Nanoscale* **2021**, 13, 912.
- [67] M. Yadav, A. Kashir, S. Oh, R. D. Nikam, H. Kim, H. Jang, H. Hwang, *Nanotechnology* **2022**, 33, 8.
- [68] M. T. Do, N. Gauquelin, M. D. Nguyen, J. Wang, J. Verbeeck, F. Blom, G. Koster, E. P. Houwman, G. Rijnders, *Sci. Rep.* **2020**, 10, 7310.
- [69] M. Kim, Y. Goh, J. Hwang, S. Jeon, *Appl. Phys. Lett.* **2021**, 119, 26.
- [70] H. J. Kim, M. H. Park, Y. J. Kim, Y. H. Lee, T. Moon, K. D. Kim, S. D. Hyun, C. S. Hwang, *Nanoscale* **2016**, 8, 1383.
- [71] A. Chouprik, M. Spiridonov, S. Zarubin, R. Kirtaev, V. Mikheev, Y. Lebedinskii, S. Zakharchenko, D. Negrov, *ACS Appl. Electron. Mater.* **2019**, 1, 275.
- [72] J. Yoon, S. Hong, Y. W. Song, J. H. Ahn, S. E. Ahn, *Appl. Phys. Lett.* **2019**, 115, 153502.